Nano Research

Open Access

Research Article

Polarization-controlled tri-state optical modulation in Au–ITO heterostructured metasurfaces via plasmon-induced hot electron injection

Zhihao Chen[1,§], Renxian Gao[1,§], Yongjun Zhang[1,§], Yaxin Wang[1], Jiahong Wen[2,5] ✉, Wenbin Chen[3], Xurong Lin[4], Ming-De Li[3] ✉, and Xiaoyu Zhao[1,6] ✉

[1] *College of Materials and Environmental Engineering, Hangzhou Dianzi University, Hangzhou 310018, China*
[2] *College of Electronics and Information, Hangzhou Dianzi University, Hangzhou 310018, China*
[3] *Guangdong Provincial Key Laboratory of Sensing Physics and System Integration Applications, School of Physics and Optoelectronic Engineering, Guangdong University of Technology, Guangzhou 510006, China*
[4] *China Circuit Technology (Shantou) Corporation Plant II, Shantou 515065, China*
[5] *Shangyu Institute of Science and Engineering, Hangzhou Dianzi University, Shaoxing 312000, China*
[6] *Zhejiang Key Laboratory of Energy Conversion Materials for Advanced Motor, Hangzhou Dianzi University, Hangzhou 310012, China*
[§] *Zhihao Chen, Renxian Gao, and Yongjun Zhang contributed equally to this work.*

Cite this article: *Nano Research*, **2026**, *19*, 94908336. https://doi.org/10.26599/NR.2026.94908336

ABSTRACT: Metal-semiconductor plasmonic metasurfaces enable precise optical field manipulation at the subwavelength scale; however, most existing designs rely on external fields and exhibit only binary responses, thereby restricting the realization of multistate logic operations. Here, we present an *in-situ* polarization-controlled approach based on an Au–indium tin oxide (ITO) bilayer nanocrescent with a Schottky heterojunction for achieving polarization-dependent tristate optical modulation. Polarization-selective excitation of distinct localized plasmon modes facilitates directional hot-electron injection across the Au–ITO interface, thereby producing three distinct programmable states—positive, zero, and negative—at a single detection wavelength. This symmetric bilayer design is applicable to other metal-semiconductor composites and offers generalizable design principles for ternary logic, multistate optical encoding, and ultrafast photonic information processing. The proposed concept is validated through both experimental measurements and numerical simulations.

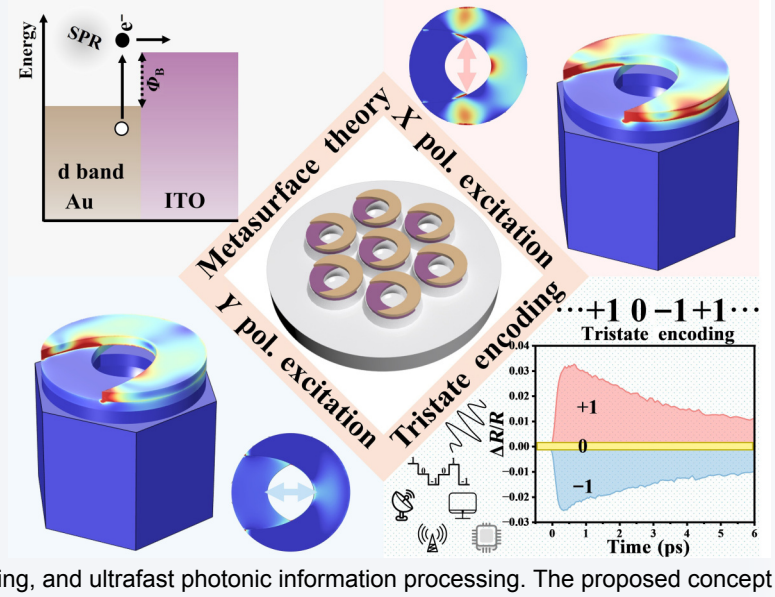

KEYWORDS: hot-electron, plasmon, optical encoding, metal-semiconductor, metasurfaces, ultrafast

1 Introduction

In the era of high-speed multidimensional electronics, traditional binary logic architectures encounter intrinsic limitations in storage density and computational efficiency. Theoretical studies suggest that multivalued logic systems, including ternary and quaternary logic, can significantly enhance information density and parallel processing capabilities by expanding the number of states per logic unit, thereby effectively addressing scalability constraints inherent to binary architectures [1–8]. In this context, plasmonic optical metasurfaces exhibit ultrafast temporal responses, enabling dynamic spatial-symmetry breaking and optical-field

Received: October 23, 2025; **Revised:** December 5, 2025
Accepted: December 11, 2025

✉Address correspondence to Jiahong Wen, wenjiahong@hdu.edu.cn; Ming-De Li, mdli@stu.edu.cn; Xiaoyu Zhao, zhaoxy@hdu.edu.cn

reconstruction on femtosecond-to-picosecond timescales. These capabilities position plasmonic metasurfaces as promising platforms for multistate all-optical modulation and integrated on-chip optical information processing. By leveraging plasmonic enhancement mechanisms, these metasurfaces provide ultrafast response times, versatile structural design flexibility, and high integration densities, rendering them particularly suitable for the development of multistate optical modulation elements [9–12].

In recent years, metasurface-based transient optical modulation has experienced substantial progress. In metallic plasmonic structures, dynamic control of optical responses has been achieved through polarization-selective excitation of distinct localized modes [13, 14]. For instance, Guo and co-workers demonstrated that indium tin oxide (ITO) nanorod arrays exhibit epsilon-near-zero (ENZ) resonance under visible-light pumping. This leads to sub-picosecond all-optical modulation and shows that pure oxide dielectrics can induce significant transmission changes via polarization-selective surface-plasmon excitation [15, 16]. Concurrently, metal-semiconductor heterojunctions have attracted attention for their enhanced photoinduced charge transfer and nonlinear response capabilities [17, 18]. Dalal et al. introduced a U-C-shaped Au–VO_2 nanocolumn heterostructure to realize a dual-wavelength plasmonic optical switch based on the VO_2 phase transition [19–22]. However, most demonstrations are limited to "on/off" binary switching or depend on external stimuli involving multiple structures or physical fields. As a result, they fail to generate tristate or higher multivalued responses *in-situ* on a single metasurface platform [23–29].

In response to these challenges, we propose and experimentally validate an *in-situ* polarization-control strategy based on an Au–ITO heterojunction metasurface. Plasmon-excitation-induced hot-electron injection from Au into ITO enables controllable, transient modulation of the local dielectric response, thereby realizing tristate all-optical modulation within a single architecture (design principle and tristate response shown in Fig. 1(a). In contrast to conventional schemes, the symmetric bilayer nanocrescent structure (model and scanning electron microscopy (SEM) image in Fig. 1(b)) enables the excitation of plasmon modes at the arm heterojunction region under *X*-polarized excitation and at the inner tip under *Y*-polarized excitation. Plasmon-induced hot-electron injection at the metal–oxide interface leads to variations in localized electron temperature (T_e) and dielectric function modulation under each polarization state. As shown in Fig. 1(a), *X*-polarized excitation modulates the transient reflectance between $\Delta R/R = 0$ and $\Delta R/R > 0$ (zero and positive states), whereas *Y*-polarized excitation switches between $\Delta R/R = 0$ and $\Delta R/R < 0$ (zero and negative states), where R denotes the equilibrium reflectivity and ΔR represents the pump-induced reflectance change. This behavior establishes three distinct optical states. Coupled COMSOL Multiphysics and two-temperature-model simulations further elucidate the causal relationships between hot-electron generation, electron-temperature dynamics, and dielectric-function evolution. This *in-situ* polarization-control approach not only overcomes the binary modulation limit but also provides theoretical foundations and structural paradigms for next-generation multivalued all-optical logic devices, multistate optical memory, and high-dimensional optical communication systems. Theoretical analysis reveals that polarization-controlled modal coupling not only reshapes the local electric field distribution but also modulates hot-electron generation, transport, and relaxation dynamics, thereby influencing the local dielectric response. These synergistic effects collectively determine the polarization-dependent tristate response observed in the Au–ITO symmetric bilayer nanocrescent metasurface (AINCM).

2 Results and discussion

Figure 1(c) presents a schematic workflow of the fabricated

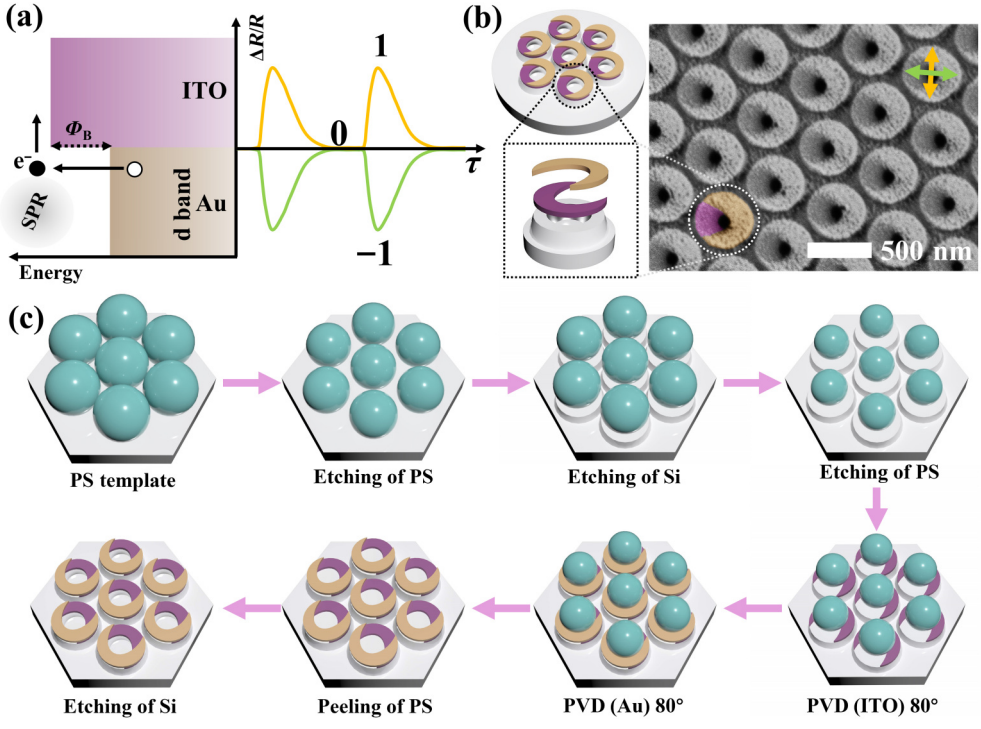

Figure 1 (a) Operating principle and tristate optical response of the AINCM. (b) Structural schematic and representative SEM image of the AINCM. (c) Schematic of the AINCM fabrication workflow.

AINCM. Polystyrene (PS) microspheres were self-assembled into a close-packed monolayer to serve as the template mask. The process then proceeded with a first reactive ion etching (RIE) step (O_2 plasma) to trim the PS spheres and expose the underlying Si, followed by an initial Si etch (SF_6 plasma) to transfer the pattern and define the inter-feature spacing. A second RIE treatment was subsequently applied to the PS spheres. Using oblique-angle physical vapor deposition (PVD) at an 80° tilt, the lower ITO layer was deposited first, and the upper Au layer was deposited subsequently in the opposing direction. After removal of the PS template, a final Si RIE step completed the formation of the AINCM. The nanocrescents form a hexagonal close-packed (HCP) lattice, with each unit having an outer diameter of approximately 500 nm and a central aperture of approximately 95 nm. In the pseudocolored SEM image, the orange (bright) regions correspond to the top Au layer, the purple regions correspond to the underlying ITO, and the central dark hole indicates the nanopore produced by template removal and subsequent Si RIE. The SEM images in Fig. S1 in the Electronic Supplementary Material (ESM) demonstrate the high uniformity of the bilayer heterojunction nanocrescents in size, morphology, and periodicity, providing a robust structural basis for the subsequent study of polarization-dependent tristate optical responses.

To investigate the femtosecond-scale ultrafast dynamics of the AINCM, we screened transient pump wavelengths by combining steady-state reflection spectroscopy with finite-element electromagnetic simulations. Figure 2(a) (red curve) presents the measured reflection spectra under *X*-polarization, in which pronounced absorption features appear near 600, 730, and 800 nm; these features are well reproduced by COMSOL Multiphysics simulations (blue curve in Fig. 2(a)). The small spectral offsets between experiment and simulation are attributed to slight geometric variations of the fabricated AINCM that are not fully captured in the model. Simulation parameters (mesh resolution, boundary conditions, and material dispersion models) are given in Fig. S2 in the ESM. To elucidate the physical origin of the three absorption peaks, three-dimensional electric-field mode distributions were extracted from COMSOL. Figures 2(b)–2(d) show that, under *X*-polarized excitation, the electric field is mainly concentrated at the coupled interface between the outer arms of the Au nanocrescents and the ITO layer (solid orange circles), producing pronounced near-field enhancement. These localized enhancements directly correspond to the absorption increases at 610, 730, and 800 nm, indicating that, for *X*-polarization, plasmonic activity at the Au–ITO arm heterojunction is dominant and promotes plasmon-induced interfacial charge transfer. Following the polarization-dependent control mechanism, we measured and simulated the reflection spectra under *Y*-polarization. Figure 2(e) exhibits clear absorption peaks at 630 and 730 nm; the corresponding near-field maps (Figs. 2(e)–2(h)) at 630, 730, and 800 nm show that, in contrast to the *X*-polarized case, the field is concentrated at the nanocrescent tips and inner-wall regions (dashed tangerine circles). Modulates hot-electron generation, transport, and relaxation dynamics, thereby influencing the local dielectric response. These synergistic effects collectively determine the polarization-dependent tristate response observed in the AINCM.

Notably, both polarization states exhibit a certain degree of tip-related field enhancement, which is likely attributed to the idealized sharp-tip geometry in the simulation, whereas the actual tips (Fig. 1(c)) are comparatively blunt. To quantify the contribution of tip hotspots, we extracted the electric field intensities at the red-dot positions indicated in Fig. S3(a) in the ESM and plotted them as a function of wavelength. The result indicates that, under *Y*-polarization, the tip region produces negligible hotspot activity, which helps to explain the weak tip contribution observed in the transient reflection spectra. Finally, to verify the essential role of the ITO layer, we compared the optical responses of a standalone Au nanocrescent structure and the AINCM. Both experimental and simulated spectra (Fig. S3(b) in the ESM) exhibit only weak absorption features in the absence of the ITO layer. Although the standalone Au nanocrescent also exhibits polarization-dependent

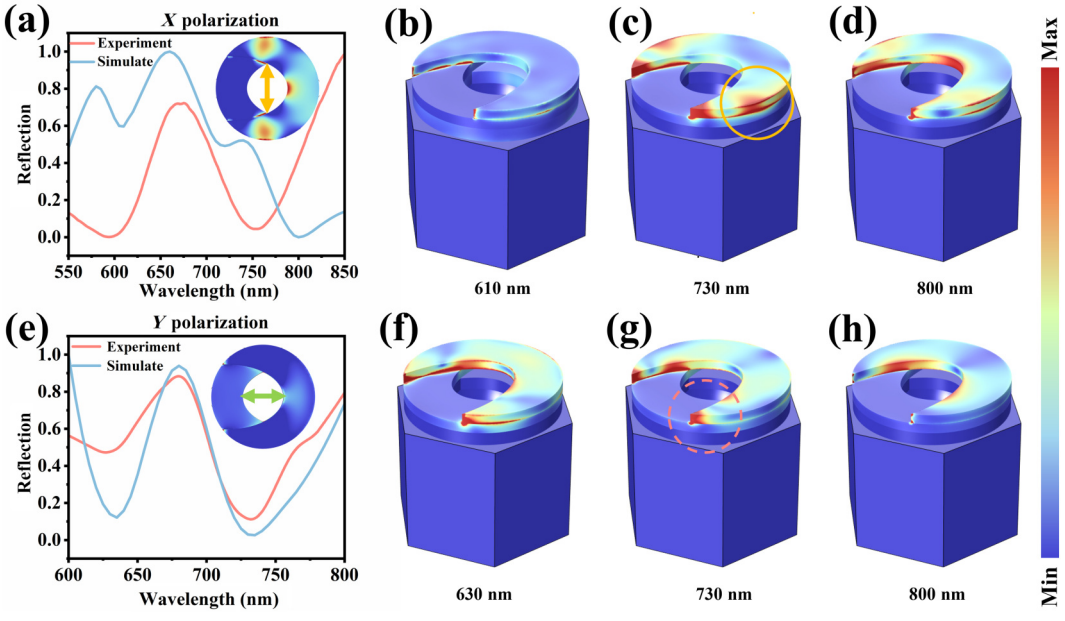

Figure 2 (a) Experiment (red) and COMSOL-simulated (blue) reflection spectra of the AINCM under *X*-polarization. ((b)–(d)) Simulated near-field (electric-field energy) distributions of the AINCM under *X*-polarization at 600, 730, and 800 nm. (e) Measured and simulated reflection spectra under *Y*-polarization. ((f)–(h)) Simulated near-field distributions under *Y*-polarization at 630, 730, and 800 nm.

field localization, these results conclusively indicate that the Au–ITO heterojunction is indispensable for modulating local electric fields and enabling plasmon-induced charge transfer.

To investigate the polarization-dependent differences in the AINCM transient reflectivity, we employed a femtosecond pump-probe setup to measure transient reflection spectra (pulse duration 84 fs; broadband pump pulses with central wavelengths of 340, 633, and 800 nm, see Fig. S4 in the ESM). As shown in Fig. 3(a), it shows a pronounced positive response ($\Delta R/R > 0$) at 730 nm under 633 nm pump excitation with *X*-polarized light. This behavior is attributed to a combination of hot-electron relaxation and interfacial injection. Following femtosecond excitation, hot electrons generated in Au undergo ultrafast electron–electron scattering (< 100 fs) [30], while a fraction overcomes the ~ 0.2 eV Au–ITO Schottky barrier (Fig. 1(a)) and is injected into ITO, driven by the interfacial electric field gradient [30–32]. Subsequent energy dissipation processes include electron–electron scattering, electron–phonon coupling (1–10 ps), and interfacial hot-electron injection. In contrast, Fig. 3(b) shows under 633 nm pump excitation with *X*-polarized light, the transient reflection at 730 nm exhibits a negative response ($\Delta R/R < 0$). Note that the data were processed to enhance spectral contrast, and the negative feature is therefore not directly visible in the plot (see Fig. S5 in the ESM). This negative response is attributed to localized "hot spots" that form away from the Au–ITO interface, thereby failing to effectively trigger interfacial charge transfer. The presence of the ITO layer enables plasmon-resonance excitation in Au to generate a high density of hot electrons while simultaneously accelerating the decay of T_e through interfacial charge transfer, thereby dynamically modulating the local dielectric function.

To evaluate the generality of this polarization-dependent behavior and examine its consistency across different excitation conditions, we further performed measurements using an 800 nm pump. As shown in Fig. 3(c), under *X*-polarized excitation, the transient response at 730 nm becomes strongly positive ($\Delta R/R > 0$), with rise and decay times closely matching those measured at the 633 nm resonance. This consistency confirms that strong field localization at the Au–ITO interface is essential for generating the positive transient response. In contrast, under 800 nm pump excitation with *Y*-polarized light (Fig. 3(d)), the transient response at 730 nm remains negative ($\Delta R/R < 0$), consistent with the results obtained at 633 nm. Figure 2(h) reveals that no significant hotspot forms at the tip under *Y*-polarized excitation. This suggests that the negative response originates from weak field enhancement along the inner walls of the AINCM, which is insufficient to drive hot-electron injection across the Au–ITO heterointerface. In addition, we supplemented correlation-based repeatability tests under 800 nm pump excitation for the AINCM, as detailed in Fig. S6 in the ESM. To verify that the polarization-dependent transient response originates from plasmon-induced charge transfer rather than from intraband or interband transitions alone, we performed supplementary measurements using a 340 nm pump (Figs. 3(e) and 3(f)). The absence of polarization dependence at 340 nm indicates that the tristate modulation mechanism fundamentally relies on the combined effects of plasmon-resonance-induced local field enhancement and interfacial charge transfer.

To quantitatively evaluate the effectiveness of polarization control, we extracted $\Delta R/R$ delay traces within the 720–745 nm range under 633 and 800 nm pump excitation with *X*- and *Y*-polarized light (Figs. 3(g) and 3(h)). For spectral visualization in the figures, we applied locally weighted estimated scatterplot smoothing (LOWESS) local regression smoothing (smoothing factor 0.2, implemented in Origin). All parameters used for kinetic fitting and threshold/state classification were determined solely from the unsmoothed raw data. The fitting time window was set to 0.2 to 5.0 ps. Under *X*-polarized excitation yields, a pronounced positive $\Delta R/R$ peak is observed at approximately 500 fs, followed by a rapid decay, whereas under *Y*-polarized excitation, the transient response remains negative throughout the delay window. This polarization-dependent behavior indicates that the AINCM selectively couples to distinct localized plasmonic modes and associated hot-electron dynamics, contingent upon the polarization state of the pump excitation. Based on the polarity and amplitude differences observed in Figs. 3(g) and 3(h), we propose a ternary optical modulation scheme, wherein modulation states of "negative",

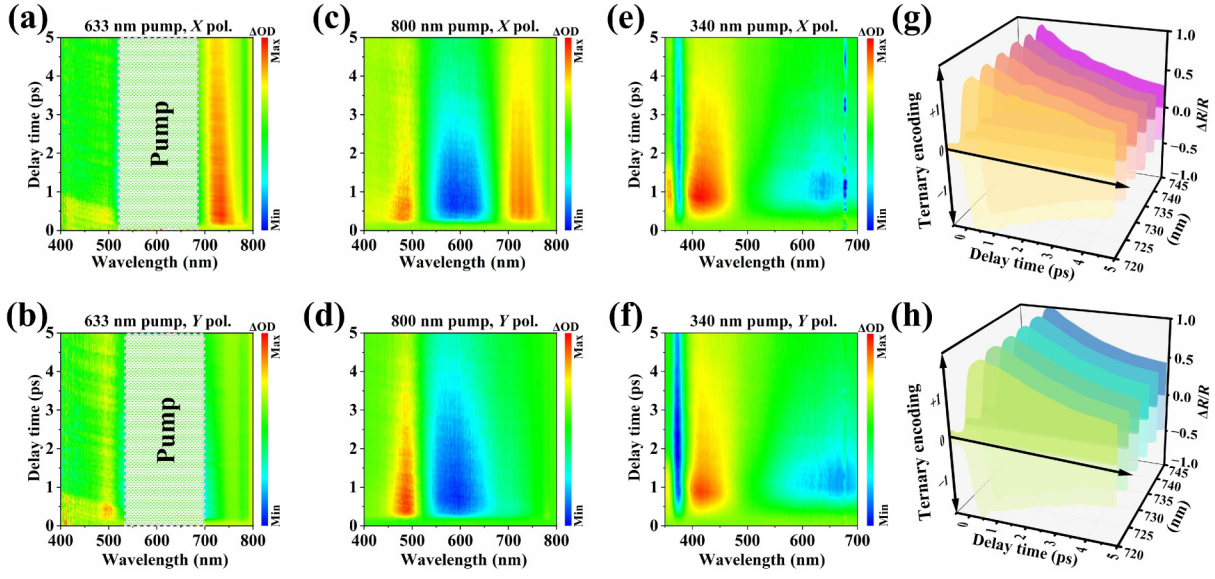

Figure 3 ((a) and (b)) Transient reflection spectra under 633 nm pump excitation with *X*- and *Y*-polarized light. ((c) and (d)) Transient reflection spectra under 800 nm pump excitation with *X*- and *Y*-polarized light. ((e) and (f)) Transient reflection spectra under 340 nm pump excitation with *X*- and *Y*-polarized light. ((g) and (h)) Time-resolved $\Delta R/R$ signals in the 720–745 nm range under 633 and 800 nm pump excitation, with *X*- and *Y*-polarized light.

"zero", and "positive" responses can be achieved at a fixed probe wavelength of 730 nm by controlling the pump polarization (*X* or *Y*). To determine the tristate behavior, we adopted a hybrid thresholding strategy based on baseline noise and relative signal amplitude, as detailed in Fig. S7 in the ESM. This capability highlights the potential of the AINCM architecture for polarization-controlled multistate optical modulation.

To investigate the hot-electron dynamics of the AINCM under different pump polarizations, we developed a coupled simulation framework integrating COMSOL Wave Optics module with a two-temperature model to compute the spatiotemporal evolution of the T_e. The Wave Optics solver was first employed to calculate the spatial distribution of electromagnetic power-loss density ($Q(x,y,z)$) within the nanocrescent. This spatially resolved absorbed power density $S(x,y,z,t)$ was then modulated by the temporal intensity profile of the pump pulse to construct the volumetric heat source term

$$S(x,y,z,t) = Q(x,y,z)I_{\text{pump}}(t) \quad (1)$$

where $I_{\text{pump}}(t)$ represents the normalized temporal intensity profile of the pump pulse.

Subsequently, the temporal evolution of the T_e and lattice temperature (T_l) were governed by the following set of coupled partial differential equations

$$C_e(T_e)\frac{dT_e}{dt} = \nabla\cdot(k_e\nabla T_e) - G(T_e - T_l) - G_2 + S(x,y,z,t) \quad (2)$$

$$C_l(T_l)\frac{dT_l}{dt} = \nabla\cdot(k_p\nabla T_l) + G(T_e - T_l) \quad (3)$$

where C_e and C_l are the electron and lattice heat capacities, respectively; t denotes time; ∇ is the nabla operator; k_e is the electron thermal conductivity; G denotes the electron–phonon coupling constant, an additional interfacial coupling term, G_2, is included to account for hot-electron diffusion into the ITO layer; and k_p is phonon (lattice) thermal conductivity. Simulation results (Fig. 4(a)) reveal the spatiotemporal evolution of T_e under 800 nm *X*-polarized excitation. The hotspots are strongly concentrated in the crescent arm regions, leading to substantial hot-electron generation and significantly elevated electron temperatures. These high-energy electrons undergo rapid thermalization, decaying within hundreds of femtoseconds via interfacial injection into the ITO layer. In contrast, under *Y*-polarized excitation (Fig. 4(b)), the hotspots are primarily distributed along the inner crescent walls, where the plasmonic coupling and local field enhancement are relatively weak, resulting in limited hot-electron generation and a modest increase in local T_e.

To quantify this difference, we extracted the temporal evolution of the average T_e at representative positions within the heterojunction arms (Fig. 4(c)). The results reveal a higher peak T_e under *X*-polarized excitation, indicating that *X*-polarization preferentially excites plasmonic modes localized at the heterojunction arms of the AINCM. These modes induce strong local field enhancement, significantly increasing the efficiency of hot-electron generation. The resulting hot electrons are rapidly injected from the Au crescent arms into the ITO layer via interfacial channels, leading to a sharp sub-picosecond decay in T_e and enabling efficient energy transfer across the interface. We also explicitly state the instrument response function (IRF = 84 fs) used in the convolution-based fitting. Convolution fits yield a fast component (τ_{rise}) that remains below = 300 fs for visible–near-infrared excitation (633 and 800 nm), consistent with rapid electron

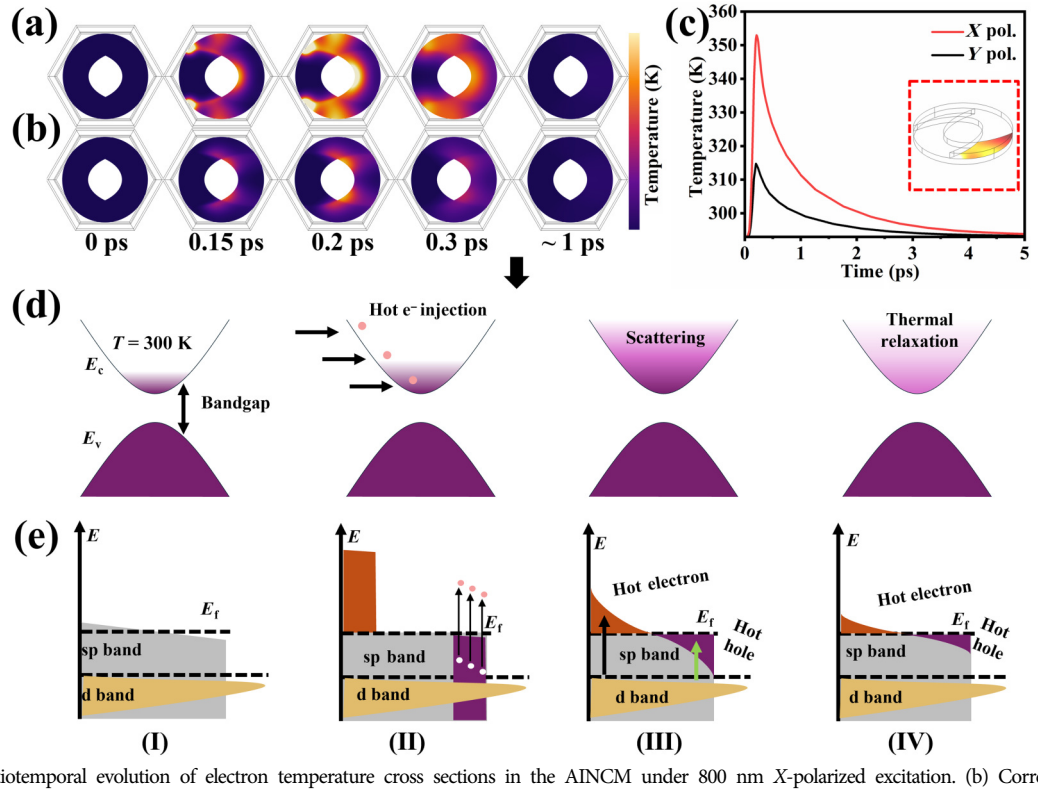

Figure 4 (a) Spatiotemporal evolution of electron temperature cross sections in the AINCM under 800 nm *X*-polarized excitation. (b) Corresponding electron temperature evolution under 800 nm *Y*-polarized excitation. (c) Temporal evolution of the electron temperature at the Au–ITO heterojunction arm under both *X*- and *Y*-polarized excitation. (d) Hot-electron dynamics in the ITO layer of the AINCM under *Y*-polarized excitation. (e) Hot-electron dynamics in the Au layer of the AINCM under *X*-polarized excitation.

thermalization and the onset of interfacial hot-electron transfer, and a slower decay component (τ_{decay}) in the 4–6 ps range, which we attribute to electron–phonon coupling and subsequent energy dissipation into the lattice and substrate. These fitted time constants agree well with the simulated hot-electron cooling dynamics shown in Fig. 4(c), further strengthening the physical interpretation of the two relaxation channels. In contrast, *Y*-polarized excitation predominantly induces hotspots along the inner walls, where interfacial hot-electron injection is negligible. As a result, the peak T_e is considerably lower, and the subsequent cooling is governed primarily by conventional electron–phonon coupling, exhibiting a slower decay. These spatiotemporal characteristics are consistent with the simulated near-field mode distributions, providing quantitative validation of the polarization-controlled spatial selectivity in hot-electron relaxation pathways.

Figures 4(d) and 4(e) provide a comparative illustration of the polarization-dependent ultrafast response dynamics of the Au–ITO heterojunction under *X*- and *Y*-polarized excitation. Based on the simulated hot-electron distribution maps at four characteristic time points, the dynamic process can be divided into four distinct stages: (I) Upon pump-pulse excitation, a nonthermal electron distribution is generated, leading to a rapid increase in the local T_e (τ_{rise} < ~ 300 fs). Concurrently, hot electrons are injected from Au into the adjacent ITO layer. ((II) and (III)) During the electron–electron and electron–phonon scattering regimes, the electronic energy undergoes redistribution, ultimately driving the system toward thermal equilibrium (electron–electron scattering and subsequent electron–phonon coupling on the sub-ps to few-ps timescales; τ_{decay} = 4–6 ps). (IV) In the cooling regime, phonon emission and heat diffusion in both Au and ITO dominate (> 10 ps). We then combine the calculated T_e with the Drude model

$$\varepsilon_{(\omega)} = \varepsilon_{\infty} - \frac{\omega_p^2}{\omega^2 + j\omega\gamma} \quad (4)$$

where $\varepsilon_{(\omega)}$ is complex permittivity (dielectric function) at angular frequency ω; ε_{∞} is high-frequency permittivity; the plasma frequency (ω_p) is defined as $\omega_p^2 = \frac{Ne^2}{\varepsilon_0 m^*}$, where N is free-electron density, ε_0 is vacuum permittivity, and m^* is effective electron mass; j is imaginary unit; and γ is damping constant. Under *X*-polarized excitation, plasmon resonance at the Au–ITO interface generates non-equilibrium hot electrons, which are injected into the ITO layer, thereby increasing its carrier concentration. The resulting carrier injection dynamically modulates the dielectric function of ITO, leading to a pronounced positive transient optical response ($\Delta R/R > 0$) at 730 nm. In contrast, under *Y*-polarized excitation, the excited plasmonic modes do not effectively localize at the Au–ITO interface, thereby suppressing interfacial hot-electron injection. As a result, hot electrons remain confined within the Au layer, and the carrier concentration in ITO remains nearly constant. Within the femtosecond probing window, changes in the imaginary part of the Au dielectric function ($Im_{(\varepsilon\_Au)}$) are minimal. This slight negative variation in $Im_{(\varepsilon\_Au)}$, induced by the thermally excited electron population in Au, gives rise to the observed negative transient reflectance signal ($\Delta R/R < 0$).

3 Conclusions

In summary, this study demonstrates polarization-dependent dynamic tristate optical responses in a heterojunction metasurface based on an Au–ITO architecture. By varying the polarization of the pump light at a fixed wavelength (730 nm), the system transitions among distinct optical states characterized by negative, zero, and positive transient signals. This multistate behavior results from the combined contributions of plasmonic field enhancement in the metal layer and interfacial hot-electron injection into the semiconductor. The underlying physical mechanisms are further elucidated through two-temperature model simulations, which capture the coupled electron-lattice dynamics. Compared to conventional designs that rely solely on either plasmonic or carrier-based effects, this hybrid strategy introduces additional degrees of freedom in optical modulation and information encoding. By leveraging polarization-tunable hot-electron dynamics at the heterojunction, the control of polarization is extended into the temporal domain, enabling a quasi-tristate transient modulation scheme. This approach transcends the binary constraints of traditional optical modulators and establishes a foundation for multilevel photonic logic, reconfigurable state switching, and high-density information processing. Moreover, it provides a potential applicability and experimental framework for metasurface-enabled multivalued optical computing. Future directions involving heterointerface barrier engineering and multilayer integration hold promise for realizing higher-dimensional tunable optical state modulation.

Electronic Supplementary Material: Supplementary material (additional SEM characterization, COMSOL simulation schematics, pump-probe experimental setup details, polarization-dependent $\Delta R/R$ dynamics, repeatability analysis, and the tristate determination methodology supporting the main results) is available in the online version of this article at https://doi.org/10.26599/NR.2026.94908336.

Data availability

All data needed to support the conclusions in the paper are presented in the manuscript and the Electronic Supplementary Material. Additional data related to this paper may be requested from the corresponding author upon request.

Acknowledgements

This work was supported by the National Natural Science Foundation of China (Nos. 12374345, U24A20103, 12404358, and 12304309), the Natural Science Foundation of Zhejiang Province (Nos. LZ26E010002 and LQN25A040010), the Key R&D Project of Zhejiang Province (No. 2024C03258), the Fundamental Research Funds for the Provincial Universities of Zhejiang (No. GK259909299001-310), and the Hong Kong Joint Laboratory for Preparation and Application of Ordered Structural Materials of Guangdong Province (No. 2023B1212120011).

Declaration of competing interest

All the contributing authors report no conflict of interests in this work.

Author contribution statement

Z. H. C.: Data curation, writing – original draft, experimental design. R. X. G.: Conceptualization, project administration, funding acquisition, writing – original draft. Y. J. Z.: Validation, project administration. Y. X. W.: Validation. J. H. W.: Project administration, funding acquisition, software (theoretical

calculations). W. B. C.: Investigation (transient optical experiments). X. R. L.: Validation. M.-D. L.: Project administration, funding acquisition. X. Y. Z.: Methodology, funding acquisition, experimental design. All the authors have approved the final manuscript.

Use of AI statement

None.

References

[1] Zhu, X. H.; Xi, M. Q.; Wang, J. Y.; Zhang, P. P.; Li, Y.; Luo, X.; Bai, L.; Chen, X. X.; Peng, L. M.; Cao, Y. et al. High-performance ternary logic circuits and neural networks based on carbon nanotube source-gating transistors. *Sci. Adv.* **2025**, *11*, eadt1909.

[2] Yu, F. L.; Chen, J.; Huang, L. J.; Zhao, Z. Y.; Wang, J. X.; Jin, R.; Chen, J.; Wang, J.; Miroshnichenko, A. E.; Li, T. X. et al. Photonic slide rule with metasurfaces. *Light: Sci. Appl.* **2022**, *11*, 77.

[3] Lee, S.; Lee, K.; Liu, C. H.; Kulkarni, G. S.; Zhong, Z. H. Flexible and transparent all-graphene circuits for quaternary digital modulations. *Nat. Commun.* **2012**, *3*, 1018.

[4] Lee, C.; Lee, C.; Lee, S.; Choi, J.; Yoo, H.; Im, S. G. A reconfigurable binary/ternary logic conversion-in-memory based on drain-aligned floating-gate heterojunction transistors. *Nat. Commun.* **2023**, *14*, 3757.

[5] Ha, S. T.; Li, Q. T.; Yang, J. K. W.; Demir, H. V.; Brongersma, M. L.; Kuznetsov, A. I. Optoelectronic metadevices. *Science* **2024**, *386*, eadm7442.

[6] Emmerich, T.; Teng, Y. F.; Ronceray, N.; Lopriore, E.; Chiesa, R.; Chernev, A.; Artemov, V.; Di Ventra, M.; Kis, A.; Radenovic, A. Nanofluidic logic with mechano-ionic memristive switches. *Nat. Electron.* **2024**, *7*, 271–278.

[7] Choi, J.; Lee, C.; Lee, C.; Park, H.; Lee, S. M.; Kim, C. H.; Yoo, H.; Im, S. G. Vertically stacked, low-voltage organic ternary logic circuits including nonvolatile floating-gate memory transistors. *Nat. Commun.* **2022**, *13*, 2305.

[8] BahmanAbadi, M.; Amirany, A.; Moaiyeri, M. H.; Jafari, K. Synergizing spintronics and quaternary logic: A hardware accelerator for neural networks with optimized quantization algorithm. *J. Supercomput.* **2025**, *81*, 669.

[9] Zhang, D.; Chen, Y.; Gong, S. C.; Wu, W.; Cai, W.; Ren, M. X.; Ren, X. F.; Zhang, S.; Guo, G. C.; Xu, J. J. All-optical modulation of quantum states by nonlinear metasurface. *Light: Sci. Appl.* **2022**, *11*, 58.

[10] Schirato, A.; Maiuri, M.; Toma, A.; Fugattini, S.; Proietti Zaccaria, R.; Laporta, P.; Nordlander, P.; Cerullo, G.; Alabastri, A.; Della Valle, G. Transient optical symmetry breaking for ultrafast broadband dichroism in plasmonic metasurfaces. *Nat. Photonics* **2020**, *14*, 723–727.

[11] Jiang, H.; Chen, Y. Z.; Guo, W. Y.; Zhang, Y.; Zhou, R. G.; Gu, M. L.; Zhong, F.; Ni, Z. H.; Lu, J. P.; Qiu, C. W. et al. Metasurface-enabled broadband multidimensional photodetectors. *Nat. Commun.* **2024**, *15*, 8347.

[12] Hu, Y. Q.; Luo, X. H.; Chen, Y. Q.; Liu, Q.; Li, X.; Wang, Y. S.; Liu, N.; Duan, H. G. 3D-Integrated metasurfaces for full-colour holography. *Light: Sci. Appl.* **2019**, *8*, 86.

[13] Wang, H.; Hu, Z. X.; Deng, J. H.; Zhang, X. C.; Chen, J. F.; Li, K.; Li, G. X. All-optical ultrafast polarization switching with nonlinear plasmonic metasurfaces. *Sci. Adv.* **2024**, *10*, eadk3882.

[14] Bin-Alam, M. S.; Reshef, O.; Mamchur, Y.; Alam, M. Z.; Carlow, G.; Upham, J.; Sullivan, B. T.; Ménard, J. M.; Huttunen, M. J.; Boyd, R. W. et al. Ultra-high-*Q* resonances in plasmonic metasurfaces. *Nat. Commun.* **2021**, *12*, 974.

[15] Li, S. Q.; Guo, P. J.; Buchholz, D. B.; Zhou, W.; Hua, Y.; Odom, T. W.; Ketterson, J. B.; Ocola, L. E.; Sakoda, K.; Chang, R. P. H. Plasmonic-photonic mode coupling in indium-tin-oxide nanorod arrays. *ACS Photonics* **2014**, *1*, 163–172.

[16] Guo, P. J.; Schaller, R. D.; Ocola, L. E.; Diroll, B. T.; Ketterson, J. B.; Chang, R. P. H. Large optical nonlinearity of ITO nanorods for sub-picosecond all-optical modulation of the full-visible spectrum. *Nat. Commun.* **2016**, *7*, 12892.

[17] Wu, K.; Chen, J.; McBride, J. R.; Lian, T. Efficient hot-electron transfer by a plasmon-induced interfacial charge-transfer transition. *Science* **2015**, *349*, 632–635.

[18] Ostovar, B.; Lee, S. A.; Mehmood, A.; Farrell, K.; Searles, E. K.; Bourgeois, B.; Chiang, W. Y.; Misiura, A.; Gross, N.; Al-Zubeidi, A. et al. The role of the plasmon in interfacial charge transfer. *Sci. Adv.* **2024**, *10*, eadp3353.

[19] Smalley, J. S. T.; Vallini, F.; Montoya, S. A.; Ferrari, L.; Shahin, S.; Riley, C. T.; Kanté, B.; Fullerton, E. E.; Liu, Z.; Fainman, Y. Luminescent hyperbolic metasurfaces. *Nat. Commun.* **2017**, *8*, 13793.

[20] Seren, H. R.; Zhang, J. D.; Keiser, G. R.; Maddox, S. J.; Zhao, X. G.; Fan, K. B.; Bank, S. R.; Zhang, X.; Averitt, R. D. Nonlinear terahertz devices utilizing semiconducting plasmonic metamaterials. *Light: Sci. Appl.* **2016**, *5*, e16078–e16078.

[21] Lv, J. W.; Han, J. H.; Han, G.; An, S.; Kim, S. J.; Kim, R. M.; Ryu, J. E.; Oh, R.; Choi, H.; Ha, I. H. et al. Spatiotemporally modulated full-polarized light emission for multiplexed optical encryption. *Nat. Commun.* **2024**, *15*, 8257.

[22] Dalal, K.; Sharma, Y. VO_2 based polarization-independent dual-wavelength plasmonic switches using U and C shaped nanostructures. *Sci. Rep.* **2025**, *15*, 4020.

[23] Yu, P.; Li, J. X.; Liu, N. Electrically tunable optical metasurfaces for dynamic polarization conversion. *Nano Lett.* **2021**, *21*, 6690–6695.

[24] Manjappa, M.; Pitchappa, P.; Singh, N.; Wang, N.; Zheludev, N. I.; Lee, C.; Singh, R. Reconfigurable MEMS Fano metasurfaces with multiple-input-output states for logic operations at terahertz frequencies. *Nat. Commun.* **2018**, *9*, 4056.

[25] Li, W. L.; Chen, B. W.; Hu, X. Y.; Guo, H. B.; Wang, S.; Wu, J. B.; Fan, K. B.; Zhang, C. H.; Wang, H. B.; Jin, B. B. et al. Modulo-addition operation enables terahertz programmable metasurface for high-resolution two-dimensional beam steering. *Sci. Adv.* **2023**, *9*, eadi7565.

[26] Jung, C.; Lee, E.; Rho, J. The rise of electrically tunable metasurfaces. *Sci. Adv.* **2024**, *10*, eado8964.

[27] He, S. C.; Wang, C. J.; Tao, J.; Tang, H. S.; Wang, Z. J.; Song, J. Z. A kirigami-based reconfigurable metasurface for selective electromagnetic transmission modulation. *npj Flex. Electron.* **2024**, *8*, 48.

[28] Cotrufo, M.; Sulejman, S. B.; Wesemann, L.; Rahman, M. A.; Bhaskaran, M.; Roberts, A.; Alù, A. Reconfigurable image processing metasurfaces with phase-change materials. *Nat. Commun.* **2024**, *15*, 4483.

[29] Abdollahramezani, S.; Hemmatyar, O.; Taghinejad, M.; Taghinejad, H.; Krasnok, A.; Eftekhar, A. A.; Teichrib, C.; Deshmukh, S.; El-Sayed, M. A.; Pop, E. et al. Electrically driven reprogrammable phase-change metasurface reaching 80% efficiency. *Nat. Commun.* **2022**, *13*, 1696.

[30] Clavero, C. Plasmon-induced hot-electron generation at nanoparticle/metal-oxide interfaces for photovoltaic and photocatalytic devices. *Nat. Photonics* **2014**, *8*, 95–103.

[31] Taghinejad, M.; Taghinejad, H.; Xu, Z. H.; Liu, Y. W.; Rodrigues, S. P.; Lee, K. T.; Lian, T. Q.; Adibi, A.; Cai, W. S. Hot-electron-assisted femtosecond all-optical modulation in plasmonics. *Adv. Mater.* **2018**, *30*, 1704915.

[32] Park, Y.; Choong, V.; Gao, Y.; Hsieh, B. R.; Tang, C. W. Work function of indium tin oxide transparent conductor measured by photoelectron spectroscopy. *Appl. Phys. Lett.* **1996**, *68*, 2699–2701.